Asian Journal of Chemistry; Vol. 35, No. 2 (2023), 277-288

ASIAN JOURNAL OF CHEMISTRY

https://doi.org/10.14233/ajchem.2023.26907

REVIEW

Direct Use of 3*d*-Transition Metal Organic Framework as Catalyst for Oxygen Evolving Reaction (OER) and Hydrogen Evolving Reaction (HER)

MRINAL SARKAR

Department of Chemistry, Derozio Memorial College, Rajarhat Road, P.O. R. Gopalpur, Kolkata-700136, India

Corresponding author: E-mail: msarkar81@gmail.com

Received: 18 October 2022; *Accepted*: 30 November 2022; *Published online*: 30 January 2023; AJC-21107

High-purity hydrogen can be produced using an effective process known as electrochemical water splitting to provide environmentally acceptable fuels. The advancement of affordable, earth-rich catalysts is the fundamental obstacle to electrochemical water splitting's wide-scale industrial applications. Oxygen evolving reactions (OERs) and hydrogen evolving reactions (HERs) are two of the processes involved in electrochemical water splitting. Widespread interest has been shown in creating efficient first-row transition metal electrocatalysts that can take the role of platinum-based electrocatalysts for both oxygen and hydrogen evolving reactions. A family of crystalline porous materials made from organic ligands and metal ions are known as metal organic frameworks (MOFs). A promising family of novel materials called MOFs has been developed for high-efficiency OER and HER electrocatalysts. Direct MOF catalysts and MOF-derived catalysts are the two divisions of MOF-based catalysts. The following are examples of MOF-derived catalysts: (i) guest@ MOF composites; (ii) hybrid materials produced by pyrolyzing MOFs; and (iii) hybrid materials created from MOFs. The best direct catalysts for OER and HER are reportedly nickel/cobalt monometallic MOF and iron-nickel/iron-cobalt heterometallic MOF. According to one theory, the breakdown of organic ligands and the formation of molecules based on water-oxidizing oxides may be a result of first-row transition MOFs being exposed to the hostile HER and OER conditions. The most recent advancements in first-row transition MOFs as direct catalysts of OER and HER are outlined in this article.

Keywords: Electrocatalysis, Metal organic framework, 3*d*-Transition metal, Oxygen evolution reaction, Hydrogen evolution reaction.

INTRODUCTION

The rapid consumption of fossil fuels and the accompanying steady deterioration of the environment have prompted a dire need for the development of new kinds of renewable energy to combat the energy and environmental problems [1,2]. Due to its many benefits, including its high energy density, recyclable nature and lack of carbon emissions, hydrogen energy is an excellent substitute for fossil fuels [3-5]. Hydrogen is mostly used in the chemical sector and while its usage as a fuel is still in its early stages, it will soon find widespread use. There are three major ways to generate hydrogen: (i) steam methane reforming: CH_4 (methane) + $2H_2O$ (steam) $\rightarrow$ $4H_2$ + CO_2 (ii) coal gasification: C (coal) + $2H_2O \rightarrow 4H_2 + CO_2$; and (iii) water electrolysis [6,7]. Although coal gasification and steam methane reforming are more affordable, they also yield CO_2 gas. Although water electrolysis is an environmental friendly and renewable process, it currently costs more to produce hydrogen than the former. As a result, significant efforts have been made to reduce the cost of water electrolysis generation.

One of the most efficient means of synthesizing H_2 is through H_2O electrolysis, which uses a simple, user-friendly apparatus and produces ultrapure hydrogen. However, effective electrocatalysts are needed for H_2O electrolysis in order to drive two important electrode processes at lesser overpotentials: hydrogen evolving reaction (HER) at the cathode and oxygen evolving reaction (OER) at the anode. The benchmark electrocatalysts for OER are noble metal oxides (IrO_2 and RuO_2), while the noble metal platinum is by far the most active element for HER [8,9]. According to a current benchmark that equates to a minimum solar to fuel conversion efficiency of 10%, the aforementioned noble catalysts perform H_2O electrolysis at a mild

This is an open access journal, and articles are distributed under the terms of the Attribution 4.0 International (CC BY 4.0) License. This license lets others distribute, remix, tweak, and build upon your work, even commercially, as long as they credit the author for the original creation. You must give appropriate credit, provide a link to the license, and indicate if changes were made.

overpotential of 400-500 mV for a benchmark current (10 mA cm^{-2}) [10-12]. However, the use of these materials in extensive commercial applications is constrained by their scarcity, instability under extended water electrolysis and high price. Therefore, novel crystalline solid materials displaying effective catalytic activity using elements found on Earth under ambient conditions must be developed as a low-cost alternative to noble metal catalysts [13,14].

Metal organic frameworks (MOFs) are a good substitute for precious metal-based catalysts due to their hierarchical surface morphology, tuneable chemical structure, vast surface area and the existence of a large number of active sites [15,16]. These materials belong to a class of the dimensionally-controllable substances produced by fine-tuning the reaction conditions for the incorporation of metal cations and organic ligands. The advantageous traits of heterogeneous catalysts are present in MOFs due to their active metal centres or pre-functionalized organic ligands [17,18]. Undoubtedly, because of their accessible pores and open channels, MOFs hold considerable promise as HER and OER electrocatalysts since they can accommodate electrolytes, promote reactant diffusion and help the transport/evolution of produced oxygen gas. Furthermore, in MOFs, the catalytically active sites are uniformly dispersed metal cations. Through changing the coordination mode or chelation in a certain way, ligands in frameworks would be able to regulate the redox switching characteristics of nearby metal cations [19]. However, the majority of MOFs have limited electrochemical water electrolysis potential due to their weak electrical conductivity [20]. A dual-site mechanism [21,22], surface hydroxylation [23], defects [24] and lattice contraction [25] are the few methods to increase the electrocatalytic activity of MOFs. Direct MOF catalysts and MOF-derived catalysts are the two groups into which MOF-based catalysts have been classified. The following are examples of MOF-derived catalysts: (i) guest@ MOF composites; (ii) hybrid materials produced by pyrolyzing MOFs; and (iii) hybrid materials created from MOFs (MOF grown as thin film on the electrode, conducting carbon-based materials act as conducting support to grow MOF, *etc*.) [26]. The direct application of first-row transition metal organic frameworks as electrocatalysts for OER and HER is the major emphasis of this review.

Mechanism of OER and HER: While comparing the kinetics of HER and OER, the first one, which contains a two-electron and two-proton transfer process, is more up-front than the latter, which encompasses a four-electron four-proton coupled process. HER can occur in acidic, basic or neutral environments and the total reaction rate is highly sensitive to the hydrogen binding energy of the surface of catalyst. The following equations show the whole HER response irrespective of pH of the solution [27-30]:

$$H^+ + M + e^- \longrightarrow M\text{–}H^* + H_2O \text{ (Volmer step)} \quad (1)$$

$$H_2O + M + e^- \xrightarrow[\text{alkali}]{\text{H–adsorption,}} M\text{–}H^* + OH^- \text{ (Volmer step)} \quad (2)$$

$$H^+ + e^- + M\text{–}H^* \xrightarrow[\text{acid}]{\text{Desorption,}} H_2 + M \text{ (Heyrovsky step)} \quad (3)$$

$$H_2O + e^- + M\text{–}H^* \xrightarrow[\text{alkali}]{\text{Desorption,}} H_2 + M + OH^- \text{ (Heyrovsky step)} \quad (4)$$

$$M\text{–}H^* + M\text{–}H^* \xrightarrow[\text{acid \& alkali}]{\text{Desorption,}} H_2 + 2M \text{ (Tafel step)} \quad (5)$$

Fig. 1 portrays a schematic illustration of different steps involved in HER *viz*. Volmer, Tafel and Heyrovsky stages in HER. The pH and the concentration of free protons are critical for H_2 production *via* water electrolysis. Proton availability in the solution will make hydrogen adsorption and desorption more efficient, which will lead to a lower applied potential for the HER. The Volmer-Tafel or Volmer-Heyrovsky routes can be followed by an appropriate catalyst depending on the work function, density of states, d-band centre and other factors. The basic difference between the Volmer-Tafel and Volmer-Heyrovsky mechanisms lies in the second step of the overall HER process, *i.e.* the desorption process. The Volmer-Tafel mechanism involves the desorption by chemical combination, whereas the Volmer-Heyrovsky process involves electrochemical desorption of H_2 molecules.

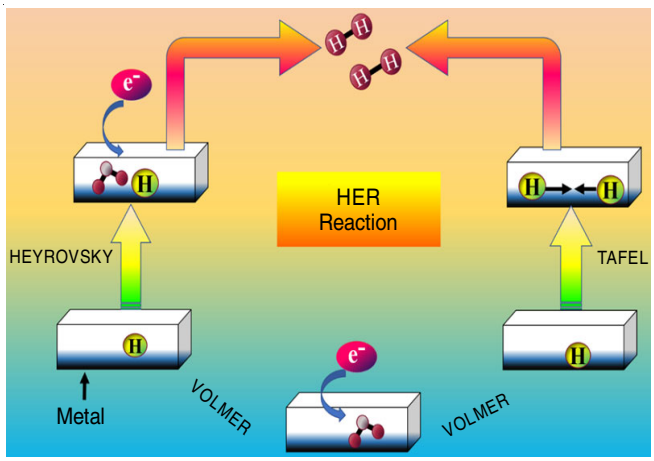

Fig. 1. Mechanism of hydrogen evolving reaction (HER) in alkaline condition

The Volmer-Tafel pathway is more likely to catalyze HER when the active site on the catalytic surface is densely packed. When compared to this, the Volmer-Heyrovsky mechanistic paths tend to be followed by catalysts having widely dispersed catalytic sites, where the distance between adjacent catalytic active sites is greater than the van der Waals radii of M-H bonds (M representing the catalytic active site). The Volmer-Tafel process is thought to be followed by catalysts with a Tafel slope value closer to 30 mV $decade^{-1}$. However, the catalyst that has a Tafel slope of 45-120 mV $decade^{-1}$ is thought to follow the Volmer-Heyrovsky mechanistic route. The mechanism and RDS (rate-determining step) of HER may be deduced from the Tafel slope, which indicates the potential difference in current density improvement on a decade scale. The Tafel slope for Pt catalysts measures 29 mV $decade^{-1}$ when the Volmer step is rapid and chemical desorption is the RDS. Tafel slope values of 39 mV $decade^{-1}$ are expected if the Volmer step is fast and electrochemical desorption is the RDS. The Tafel slope is 116 mV $decade^{-1}$ if the Volmer step is RDS. The mechanistic processes vary according to the materials utilized and their

capacity to bind hydrogen over the catalyst, which impacts the rate of H_2 evolution. A 'Volcano plot' can reveals the type of H-binding. The binding and cleavage of hydrogen in HER must be just right in energy for the ongoing evolution of the ideal catalyst. For rapid H_2 evolution, the ΔG_{H^*} must be zero under ideal conditions with the maximum j_0 value, as stated by the Sabatier principle. The Volcano type plot was obtained by using theoretically generated ΔG_{H^*} and j_0 values. When the ΔG_{H^*} is zero, the catalyst has the highest possible j_0 value, indicating high activity. The H* adsorption is weak and increases j_0 values exponentially with decreasing ΔG_{H^*} values if ΔG_{H^*} exceeds zero. When ΔG_{H^*} is less than zero, H* adsorption is strong and j_0 values decrease exponentially as ΔG_{H^*} decreases. According to the Volcano plots depicted in Fig. 2, the H-binding is influenced by changes in ΔG_{H^*} and j_0 values as well as their influence on H_2 evolution. High current density and j_0 values result in excellent hydrogen binding and facile H_2 release from the surface [31-33].

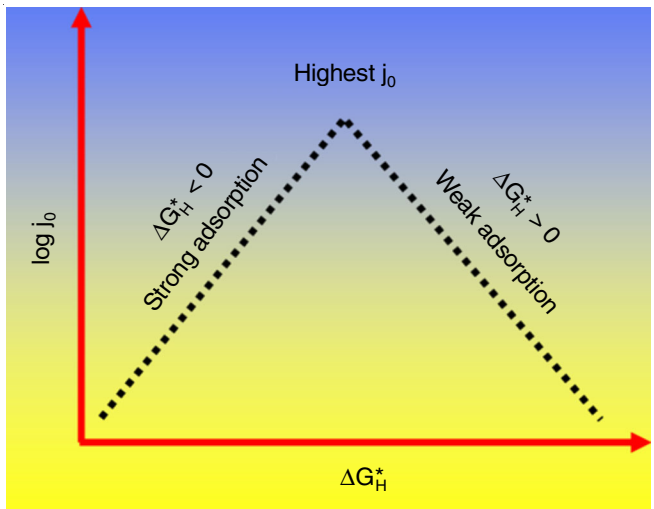

Fig. 2. Volcano plot portraying the variance of H-binding capabilities for hydrogen evolving reaction (HER)

It's noteworthy to examine eqns. 1 and 2 for the first step of acidic and alkaline HER, where in the acidic instance, active H^+ ions are adsorbing on easily accessible water molecules, but in the alkaline situation, these H^+ ions must break or dissociate the water molecules in order to adsorb. Because of this, the water dissociation process is critical to the Volmer step's effectiveness in alkaline HER. Alkaline HER can be seen from the Volmer-Heyrovsky steps that the interface is given an additional load, which is the water dissociation step as long as the free proton is accessible to continue the reaction forward. As a result, the slope of HER in alkaline solution is much steeper than the slope of HER in acidic solution. Hydroxide ions, which are formed near the electrode surface, would reduce the effective concentration of H_2O and drive water back into forward equilibrium, which is another key aspect to consider. Metal hydroxides from non-precious metals have recently found their way into alkaline water electrolysis. Pre-catalysts, rather than actual OER/HER catalysts, have been found in transition metal-based hydroxides due to the fact that hydroxide ions are easily replaced by electroactive hydroxide ions at high alkaline conditions. A metal hydroxide surface with the proper electrical structure and enough binding strength is necessary for effective alkaline hydroxide HER. Lattice hydroxide anions are predicted to promote water dissociation by allowing initial water adsorption with the partial negative charge that it possesses due to the hydrogen bonding. This is expected to occur more often.

Following the mechanism of OER, it is important to note that the pathways involved are more complex than in the case of HER. Due to the four-electron, four-proton transfer process and the complicated mechanistic results of OER, the successful commercialization of alkaline electrolyzers is wholly dependent on the effectiveness of their anodic counterparts. When it comes to the electrolyte solution utilized for OER, the mechanistic processes are generally varied. Fig. 3 depicts the mechanistic consequences in an alkaline medium as well as the overall mechanistic processes (eqns. 6-11) (where S represents the catalytic active centre).

$$S + H_2O \xrightarrow{\text{Acid}} S\text{-}OH + H^+ + e^- \quad (6)$$

$$S\text{-}OH \xrightarrow{\text{Acid}} S\text{-}O + H^+ + e^- \quad (7)$$

$$2S\text{-}O \xrightarrow{\text{Acid}} 2S + O_2 \quad (8)$$

$$S + OH^- \xrightarrow{\text{Alkali}} S\text{-}OH + H^+ + e^- \quad (9)$$

$$S\text{-}OH + OH^- \xrightarrow{\text{Alkali}} S\text{-}O + H_2O + e^- \quad (10)$$

$$2S\text{-}O \xrightarrow{\text{Alkali}} 2S + O_2 \quad (11)$$

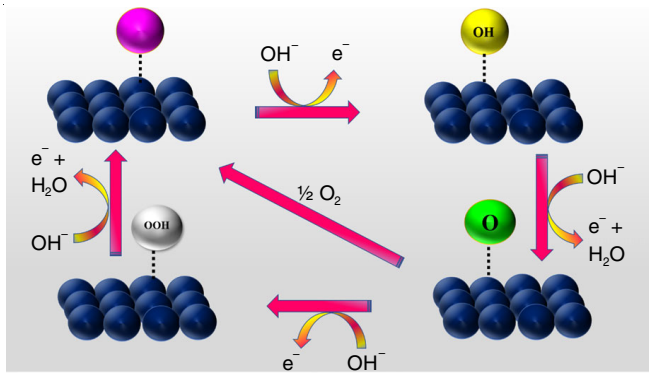

Fig. 3. Mechanistic pathways for oxygen evolving reaction (OER) in alkaline condition

In an alkaline environment, further reactions occur *via* the formation of metal oxide or metal oxyhydroxide intermediates after the M-OH bond has been formed. The entire overpotential of the catalytic H_2O oxidation process is determined by the mechanism of RDS. Therefore, it is important to take into account the efficient production of S-O bonds at the optimal bond energy while developing an electrocatalyst, *i.e.* bond energy must be neither too high nor too low [34-37].

Homometallic MOFs

Ai *et al.* [38] prepared a MOF from cobalt(II) acetate tetrahydrate and citric acid through a solvothermal pathway. Its specific surfaces have been calculated to be 924 $m^2\ g^{-1}$ for the BET area and 936 $m^2\ g^{-1}$ for the Langmuir area. It needs 408 mV over-potential for a conventional current of 10 mA cm^{-2}.

It has a Tafel value of 77 mV decade^{-1}. During 7 h of constant testing, there is a modest decrease in the catalytic current density into 1 M KOH. As the concentration of KOH solution has been increased, it has become much more electrocatalytically active. In the OER method, gradually it converts to CoOx. Huang *et al.* [39] reported two distinct kinds of cobalt based catalysts (BMM-11 and BMM-12) *via* solvothermal reactions. A conventional current of 10 mA cm^{-2} has been achieved by BMM-11 with just 362 mV overpotential and BMM-12 requires 393 mV. The Tafel slope of BMM-11 is 105.23 mV decade^{-1}, but BMM-12 has 178.07 mV decade^{-1}. The amperometric curve of BMM-11 and BMM-12 indicates no obvious degradation over a period of 10 h, indicating the electrocatalytic stability is favourable. Throughout the OER procedure, the metal organic frameworks will break down into $Co(OH)_2$ and CoOOH nanosheets.

Guan *et al.* [40] synthesized binuclear Co-based MOF (Co_2-tzpa) by reacting Co^{2+} ions with 5-(4-(tetrazol-5-yl)phenyl)-isophthalicacid under solvothermal conditions. The MOF has a BET area of nearly 228.7 m^2 g^{-1}. With a small overpotential of 336 mV, it exhibits good OER activity into 1 M KOH solution. It has a Tafel value of 58 mV decade^{-1}. It was supported on a graphite plate to determine its stability and established that the current density only shows a very little deterioration during the 25 h of electrocatalytic process. Biradha *et al.* [41] designed two MOFs termed as $\{[Ni(L)(TA)(H_2O)]\cdot 5H_2O\}_n$, TA-MOF and $\{[Ni(L)(NH_2TA)(H_2O)]\cdot DMF\cdot 3H_2O\}_n$, NH_2TA-MOF by the solvothermal reactions. A current of 1 mA cm^{-2} has been achieved by TA-MOF with just 382 mV overpotential and 356 mV is necessary for NH_2TA-MOF. The TA-MOF and NH_2TA-MOF have Tafel slope values of 94 and 105 mV decade^{-1}, respectively, which indicate the remarkable electrocatalytic activity of these two MOFs. A chronoamperometry examination was performed into 0.1 M KOH solution for the stability test of NH_2TA-MOF. Upon 12000 sec of continuous observation, a minor reduction in catalytic current density was observed. The decrease in the MOF's catalytic active sites may be to blame for the drop in catalytic current density. Bubbles of oxygen gas formed during the oxygen evolving reaction block the active sites of MOF.

Co-BPDC/Co-BDC-3 (Cat1) electrocatalyst (58.2 m^2 g^{-1}) has a greater BET area than a separate Co-BDC (Cat2, 17.9 m^2 g^{-1}) or Co-BPDC (Cat3, 39.1 m^2 g^{-1}) as reported by Ni *et al.* [42]. The larger BET surface is advantageous for enhancing its prospective catalytic activities. For a conventional current (10 mA cm^{-2}), Cat3, Cat2, the combination of Cat2 and Cat3 and Cat1 need 428 mV, 392 mV, 387 mV and 335 mV of overpotentials, respectively. Higher advantageous OER kinetics of MOFs are frequently indicated by a lower value of Tafel slope. The Tafel slope values for the MOFs are as follows: Cat3: 78.8 mV decade^{-1}, Cat2: 77.2 mV decade^{-1}, combination of Cat2 and Cat3: 81.7 mV decade^{-1} and Cat1: 72.1 mV decade^{-1}. The Cat1 electrocatalyst shows high stability. After showing 80 h of constant electrocatalytic activity, the overpotential marginally rose. After constant catalyzing for 80 h, CoOOH's diffraction peaks notably grew, indicating that CoOOH actually served as an electrocatalyst. Lin *et al.* [43] investigated that into 0.2 M phosphate buffer (pH 6.8), OER has an overpotential of 900 mV at an uncoated glassy carbon electrode. In the presence of $Co(L)_{0.5}$(adip), the overpotential is reduced to 460 mV, which indicates the good catalytic property of the MOF. The durability of MOF is tested through examining the powder X-ray diffractions produced after 2 h of controlled potential electrolysis. The morphology of $Co(L)_{0.5}$(adip) following 2 h of controlled potential electrolysis is changed slightly. The $(Co_2(L)_2(5\text{-bdc})_2(H_2O)_2\cdot H_2O$ also decreases potential from 900 mV to 570 mV demonstrated that it also exhibits electrocatalytic activity by generating oxygen from H_2O.

Qin *et al.* [44] prepared four Co-MOFs having 1,5-bi(imidazolyl)anthracene and two dibenzobarrelene based dicarboxylic acids. Among them $\{[Co_2(L_1)_2(L_2)_2\cdot(H_2O)_2]_n\cdot 3H_2O\}$ (MOF1), $\{[Co_2(L_1)_2(L_3)_2(H_2O)_2]_n\cdot 4H_2O\}$ (MOF2) and $\{[Co(L_1)_2(HL_3)_2]_n\cdot 2CH_3CN\}$ (MOF3) show 2D networks, whereas $\{[Co(L_1)(HL_3)_2\cdot(H_2O)_2]_n\}$ (MOF4) produces a one dimensional chain structure. The porosity of the MOF1, MOF2 and MOF3 has been estimated through nitrogen adsorption at 77 K. The BET surfaces for the three MOFs have been calculated as 13.694 m^2 g^{-1} for MOF1, 10.485 m^2 g^{-1} for MOF2 and 4.194 m^2 g^{-1} for MOF3. MOF1, MOF2, MOF3 and MOF4 exhibit catalytic properties having overpotentials of 411, 406, 438 and 398 mV for gaining benchmark current (10 mA cm^{-2}), respectively. The Tafel values were calculated to be 58 mV decade^{-1} for MOF1, 62 mV decade^{-1} for MOF2, 60 mV decade^{-1} for MOF3 and 59 mV decade^{-1} for MOF4, respectively and used to calculate the OER kinetics of the four MOFs. The values indicate that MOF4 exhibits good kinetics for catalyzing oxygen evolving reactions. The nearly identical powder X-ray diffraction signals obtained after 2 h dipped into 1 M KOH indicate that the crystallinity and durability of four MOFs have been maintained. Wang *et al.* [45] established that $[Co_5(^i\text{BuOip})_4(\mu_3\text{-O})(bpp)_2(DMF)(H_2O)_3]\cdot 2H_2O$ displays 340 mV overpotential for a benchmark current (10 mA cm^{-2}) in 0.5 M Na_2SO_4 electrolyte. A lesser Tafel value (130 mV decade^{-1}) is displayed by the catalyst and demonstrated an effective charge transfer. The catalytic durability was examined by chronoamperometry. In 0.5 M Na_2SO_4 electrolyte, it retains constant current density for 14 h with very little degradation, indicating high durability against oxygen evolving reaction. Wei *et al.* [46] generated a $Co(TCNQ)_2$ arrangement with a sawtooth pattern on Co foil ($Co(TCNQ)_2$/Co) serves as an OER electrocatalyst. For a current of 15 mA cm^{-2} into 1.0 M KOH, the MOF requires 310 mV overpotential. The Tafel slope value of the MOF has been obtained at 76 mV decade^{-1}, that suggests good electrocatalytic kinetics. Another important factor to consider when assessing the effectiveness of an electrocatalyst is stability. The MOF has great stability, as evidenced by the fact that its electrocatalytic property can be sustained for a minimum of 20 h. Following electrocatalytic activity, the nanoarray characteristic remains present.

In order to study the catalytic property, Lu *et al.* [47] placed $[Co_{1.5}(tib)(dcpna)]\cdot 6H_2O$ upon a GCE with the help of Nafion binder. The MOF's catalytic property improves when the KOH solution concentration is increased suggested a greater KOH concentration is advantageous to enhance the oxygen evolving reaction. The MOF exhibits greater electrocatalytic property into 1 M KOH with 360 mV overpotential at 10 mA cm^{-2}.

The Tafel values have been used for calculating the kinetics of electrocatalysis. The Tafel value for MOF has been estimated to be 89 mV decade^{-1}. The cyclic voltammetry has been used to test the durability into 1 M KOH. The fact that there are no visible variations in current density beyond 100 cycles indicates that MOF is stable. Wang *et al.* [48] observed that the surface area for Co-MOF$_{6\,h}$ (26.1 m^2 g^{-1}, produced *via* hydrothermal reaction of 6 h) is slightly bigger in comparison to Co-MOF$_{24\,h}$ (22.3 m^2 g^{-1}, generated through hydrothermal reaction of 24 h) and Co-MOF$_{72\,h}$ (18.1 m^{2}g^{-1}, produced *via* hydrothermal reaction of 72 h), respectively. As hydrothermal reaction duration increases, the MOF's surface area steadily decreases. In comparison to the overpotentials of Co-MOF$_{6\,h}$ (418 mV) and Co-MOF$_{24\,h}$ (419 mV), Co-MOF$_{72\,h}$ exhibits a comparatively smaller overpotential of 387 mV. Greater electrocatalytic activity is evidenced by a lower value of Tafel slope, which also supports that the higher the potential, the higher the reaction rate. Co-MOF$_{72\,h}$ (90 mV decade^{-1}) has a little bit lower value of Tafel slope in comparison to Co-MOF$_{24\,h}$ (91 mV decade^{-1}) and Co-MOF$_{6\,h}$ (94 mV decade^{-1}). The constant durability examination shows Co-MOF$_{72\,h}$ remains steady after three thousand seconds. It appears that Co-MOF$_{72\,h}$ maintains strong electrocatalytic activity after 1 h.

Behera *et al.* [49] synthesized [$Co_4(BTC)_3(BIM)_6$] *via* solvothermal reaction with $Co(OAc)_2{\cdot}4H_2O$ and a combination of benzene tricarboxylic acid and benzimidazole. For a conventional current (10 mA cm^{-2}), it just requires 280 mV of overpotential. The Tafel plot is produced using the polarization curves and the Tafel value has been determined to be 51 mV decade^{-1}. The chronopotentiometry method has been used to determine the MOF's stability. It exhibits a slight increase in overpotential beyond 13 h of electrocatalytic activity. The unchanged diffraction signals of the MOF were obtained from the XRD study following the oxygen evolving reaction. The MOF's outstanding durability throughout OER in an alkaline solution is shown by a little deformation in morphology. Mohan *et al*. [50] exhibited the electrocatalytic capability of Ni-MOF (BTC) (BTC = 1,3,5-benzenetricarboxylic acid) prepared at room temperature. The MOF (8.39 m^2 g^{-1}) is evidently less porous than NiO (synthesized *via* wet chemical method, 22.49 m^2 g^{-1}), as seen by its smaller BET area. At 346 and 393 mV of overpotential, respectively, the Ni-MOF and NiO catalysts were able to produce a benchmark current of 10 mA cm^{-2}. The Tafel value for Ni-MOF is calculated to be 64 mV decade^{-1} while for NiO the value is 69 mV decade^{-1}. The lesser Tafel value of the MOF indicates that it is more catalytically active in comparison to NiO. During the study periods of 10 (small scale test) and 50 h (large scale test), the electrocatalytic performance was shown to be steady. Prior to OER, the MOF looked like a light green colour, but following chronopotentiometry, it became black. The MOF underwent a change in morphology from a rough to a smooth, flake-like fine surface. Throughout the oxygen evolving reaction, due to the oxidation reaction in the anode, the MOF is converted to $Ni(OH)_2$/NiOOH.

Lin *et al.* [51] synthesized [$Co_4L_2(4,4'$-bpy)$(H_2O)_6$]·3.5 H_2O (MOF1) and [Co_2L(azene)$(H_2O)_3$]·DMF (MOF2) through utilizing a carboxylate compound. MOF1 exhibits catalytic performance through hydrogen evolving reaction for an overpotential of 460 mV. For OER, MOF1 needs 430 mV overpotential. The durability of MOF1 is tested through PXRD analysis following 2 h of controlled potential electrolysis. The pre-electrolysis and post-electrolysis PXRD peaks of MOF1 are identical, but the crystalline nature and morphology of MOF1 are slightly changed following 2 h of electrolysis. A 140 mV overpotential is required for MOF2 to synthesize hydrogen through catalytic oxidation of water. MOF2 also shows oxygen evolving reaction performance for which it needs 230 mV overpotential. The above results reflect that MOF2 exhibits greater catalytic efficiency in comparison to MOF1. Budnikova *et al.* [52] designed Zn(fcd*H*p) (MOF1) and Co(fcd*H*p) (MOF2) using $Zn(NO_3)_2{\cdot}6H_2O$ or $Co(NO_3)_2{\cdot}6H_2O$ and 1,1′-ferrocenylenbis-(H–phosphinic) acid through utilizing $(CH_3)_2NC(O)H$ solvent and CH_3OH combination. MOF1 and MOF2 catalyze the hydrogen formation process. For benchmark current (10 mA cm^{-2}) MOF1 needs 340 mV while MOF2 requires 450 mV overpotential in 1 N H_2SO_4. The values of Tafel plots were estimated at 110 mV decade^{-1} for MOF1 and 120 mV decade^{-1} for MOF2. Both MOFs exhibit electrocatalytic activity up to one thousand cycles with a slight decrease in activity. The MOFs did not alter their morphology throughout the week in water. In 1 N H_2SO_4 medium, MOF1 degrades slightly following one week, while MOF2 follows a day.

Anthony *et al.* [53] synthesized Cu-MOF with N-(-2-hydroxybenzyl)alanine using the unique effect of Co^{2+}/Ni^{2+}. Two distinct Cu-MOFs were produced as a result of Ni^{2+} ions present in the reaction medium, H_2O bound [$(Cu_2(HBA)_2(OH_2)$] (MOF1, asymmetric unit) and without H_2O bound [$(Cu_2(HBA)_2$] (MOF2, asymmetric unit). Only Cu-MOF (MOF2) without H_2O coordination was prepared by the presence of Co^{2+} ions in the reaction medium. The MOF1 needs only 417 mV overpotential for conventional current (10 mA cm^{-2}), whereas the combination of MOF1 and MOF2 needs a 465 mV into 1 M KOH solution. For MOF2 with conventional current (10 mA cm^{-2}), the greatest overpotential of 535 mV is required. An essential characteristic of catalytic MOFs is the value of Tafel plot, which is used to assess the HER's rate determination step. The combination of MOF1 and MOF2 exhibits a somewhat greater Tafel value (121 mV decade^{-1}), whereas MOF1 displays a lesser Tafel value (98 mV decade^{-1}). The maximum value of Tafel plot was observed in MOF2, which is 145 mV decade^{-1}. According to MOF1 durability analysis, it remains durable for more than 12 h without experiencing a substantial decrease in activity. He *et al.* [54] used pyrazole-3,5-dicarboxylic acid and 1,10-phenanthroline to synthesize Cu-MOF ([$Cu_3(pdc)_2(phen)_2(H_2O)_2$] = asymmetric unit) under hydrothermal conditions. The BET area of the MOF was found to be 18.7 m^2 g^{-1}. At 10 mA cm^{-2}, the potential moved through 440 mV because of the little loading of MOF in the electrode, demonstrated a considerably improved catalytic efficiency of MOF towards the hydrogen formation process. The strong durability of MOF is demonstrated through 8 h of catalytic performance. The MOF has a Tafel value of 60 mV decade^{-1}.

Xu's group [55] prepared NTU-33 crystal (asymmetric unit = [$Cu_2(NL)_2{\cdot}4H_2O$]·*x*Solvent) from 5-(pyridin-4-yl)isophthalic

acid (H_2NL) utilizing copper(II) bromide by solvothermal method. Crystals of NTU-33 were dispersed in acetone before being treated in an ultrasonic bath to form nanosheets of NTU-33. For gaining benchmark current (10 mA cm^{-2}), NTU-33 nanosheets need 560 mV overpotential, that is less than the overpotential required for the NTU-33 nanoparticles. The other crucial factor for assessing the MOF's kinetic efficiency is its value of Tafel slope. The Tafel slope value for the NTU-33 nanosheet was calculated to be 158 mV $decade^{-1}$. The nanosheet was demonstrated to be a stable and effective catalyst in an acidic solution over lengthy electrolysis for 10 h. The $[Co(OH)_2(C_8H_4O_4)]$ (CoBDC) from $Co(NO_3)_2{\cdot}6H_2O$ and terephthalic acid is synthesized by Li *et al*. [56]. In order to prepare MOFs with missing linkers, carboxyferrocene (Fc, ferrocene-carboxylic acid) was added to CoBDC. In CoBDC-$Fc_{0.17}$, the proportion of BDC:Fc is roughly 6:1. In comparison to CoBDC (17.12 $m^2\ g^{-1}$), CoBDC-$Fc_{0.17}$ exhibited a reduced BET area of 16.03 $m^2\ g^{-1}$. The Co(II) is tetracoordinated (4.4) in CoBDC–$Fc_{0.17}$ while it is nearly hexacoordinated (6.2) in CoBDC. Such findings generated the coordinatively unsaturated Co(II) upon the introduction of the missing linkers, which are anticipated to serve as catalytic sites. The CoBDC exhibits oxygen formation reaction activity for 378 mV overpotential at benchmark current (10 mA cm^{-2}). CoBDC-$Fc_{0.17}$ demonstrated the better catalytic capability for 291 mV overpotential to gain benchmark current (10 mA cm^{-2}) and has a lower value of Tafel slope (61 mV $decade^{-1}$). The CoBDC–NF (CoBDC loaded over nickel foam) exhibits outstanding catalytic activity towards oxygen formation reaction for 252 mV overpotential at 10 mA cm^{-2}. The CoBDC–Fc/NF (CoBDC–Fc deposited upon nickel foam) demonstrates massively increased oxygen formation reaction performance for extremely smaller 178 mV overpotential at 10 mA cm^{-2}. In comparison to CoBDC/NF (63 mV $decade^{-1}$), CoBDC-Fc/NF displays a reduced Tafel value (51 mV $decade^{-1}$) suggested improved oxygen formation reaction kinetics. In an extended chronopotentiometry study that lasted 80 h at a steady current of 100 mA cm^{-2}, CoBDC-Fc/NF demonstrates excellent stability.

Biradha *et al.* [57] designed four catalysts $\{[Co(L_1)(TA)(H_2O)_2]{\cdot}2H_2O\}_n$, MOF1, $\{[Ni(L_1)(TA)(H_2O)_2]{\cdot}2H_2O\}_n$, MOF2, $\{[Co(L_2)_2(TA)]{\cdot}4H_2O\}_n$, MOF3 and $\{[Ni(L_2)_2(TA)]{\cdot}4H_2O\}_n$, MOF4 by the solvothermal reactions. They also synthesized two copper-MOFs, Cu@MOF1 and Cu@MOF3, by dipping the smashed crystals of MOF1 and MOF3 individually in a 0.1 M copper(II) nitrate solution in ethanol. At 1 mA cm^{-2}, six MOFs need 370 mV for MOF2, 400 mV for MOF4, 410 mV for Cu@MOF1, 420 mV for Cu@MOF3, 420 mV for MOF1 and 430 mV overpotential for MOF3. Therefore, MOF2, having the smallest overpotential of 370 mV, exhibits the highest catalytic activity between all the MOFs. All the MOFs show significant stability since they produce the same kind of linear sweep voltammetry plot following one thousand cycles. Tafel values were estimated at 101.90 mV $decade^{-1}$ for MOF2, 120.53 mV $decade^{-1}$ for MOF4, 122.19 mV $decade^{-1}$ for Cu@MOF1, 123.00 mV $decade^{-1}$ for Cu@MOF3, 126.13 mV $decade^{-1}$ for MOF1 and 131.66 mV $decade^{-1}$ for MOF3. Between the MOFs, MOF2 has the smallest Tafel value suggested the greatest catalytic activity. The inductively coupled plasma mass spectroscopy study following the durability check exhibits no metal ions that can be detected, therefore excluding the probability of metal ions escaping from the MOF. Chen *et al.* [23] synthesized $[Co_2(\mu\text{-}Cl)_2(btta)]$ (MAF-X27-Cl) by dissolving a mixture of $CoCl_2{\cdot}6H_2O$ and 1*H*,5*H*-benzo(1,2-d:4,5-d′)bistriazole in a mixture of DMF-methanol-HCl. Chloride ion from $[Co_2(\mu\text{-}Cl)_2(btta)]$ is replaced by hydroxide ion, when it is taken into 1 M KOH for 24 h and $[Co_2(\mu\text{-}OH)_2(bbta)]$ (MAF-X27-OH) is produced. Langmuir areas were calculated to be 1407 $m^2\ g^{-1}$ for chloride bridge MOF and 1514 $m^2\ g^{-1}$ for hydroxide bridge MOF. Through contrasting the catalytic efficiency of OERs for chloride bridge MOF and hydroxide bridge MOF, the utility for bridging hydroxide is shown. Chloride bridge MOF exhibits quite weak catalytic performance; it needs 570 mV overpotential at 0.028 mA cm^{-2} (pH 7). Hydroxide bridge MOF is required for 489 mV overpotential at 2.0 mA cm^{-2} (pH 7). When pH is 14 and hydroxide bridge MOF is loaded onto a glassy carbon electrode, the hydroxide bridge MOF requires 387 mV overpotential at 10 mA cm^{-2}. Hydroxide bridge MOF shows significant stability for oxygen evolving reactions.

Li *et al.* [58] synthesized $[Ni_4(OH)_2(NDC)_3(H_2O)_2]{\cdot}2H_2O$ (Ni-MOF) by reacting 1,4-naphthalenedicarboxylic acid, nickel(II) nitrate and sodium hydroxide in ethanol/water. The use of acetylene black (AB) will increase the conductance and catalytic activity of the OER of pristine nickel MOF. The AB powder was combined into the MOF and the combination is crushed evenly to achieve AB and the nickel MOF hybrid material. In comparison to pristine nickel MOF, which has a surface area of 4.2 $m^2\ g^{-1}$, the AB and nickel MOF hybrid material has a bigger surface area of 38.5 $m^2\ g^{-1}$. The AB and nickel MOF hybrid material (supported upon a GCE) provides enhanced electrocatalytic capability, having 379 mV overpotential at 10 mA cm^{-2}, that is less in comparison to 456 mV overpotential for pristine nickel MOF. The AB and nickel MOF (supported upon a fluorine-doped tin oxide electrode) hybrid material shows the catalytic activity towards OERs, having 282 mV overpotential at 10 mA cm^{-2} and its Tafel value is 66 mV $decade^{-1}$. The electrocatalytic capability of AB and nickel MOF (supported over nickel foam electrode) hybrid material is revealed through 263 mV overpotential, is required at 10 mA cm^{-2}. It has 65 mV $decade^{-1}$ of Tafel value. The stability test for AB and nickel MOF hybrid material exhibits barely any degradation over the course of 12 h. After oxygen evolving reaction, the powder X-ray diffraction study exhibits that β-nickel(II) hydroxide is present along with nickel MOF. The characteristic parameters based on OER and HER reactions in homometallic MOFs are summarized in Table-1.

Heterometallic MOFs

Xu *et al.* [59] investigated the catalytic efficiency for Co_xFe_{1-x}-MOF-74 ($0 < x \leq 1$) against OER into 1 M KOH. Between the MOFs, $Co_{0.6}Fe_{0.4}$-MOF-74 shows the highest catalytic performance for 280 mV overpotential at 10 mA cm^{-2}. Between all the MOFs containing various iron contents, $Co_{0.6}Fe_{0.4}$-MOF-74 exhibits the lowest 56 mV $decade^{-1}$ of Tafel value, indicating the excellent kinetics of the electrocatalytic process. The durability of this heterometallic MOF was investigated through chrono-

TABLE-1
HOMOMETALLIC MOFs BASED ELECTROCATALYSTS

Electrocatalyst/Electrode	Dimension/surface area ($m^2 g^{-1}$)	Overpotential η_x (mV), x = current density (mA cm^{-2})	Slope of Tafel plot (mV $decade^{-1}$)	pH/ Electrolyte	Catalyzes	Ref.
{[$KCo_3(C_6H_4O_7)(C_6H_5O_7)(H_2O)_2$]·$8H_2O$}n(UTSA-16)/GCE	3D/924 (BET); 936 (Langmuir)	η_{10} = 408	77	1.0 M KOH	OER	[38]
[$Co(III)_2(HCOO)_2(BPTC)$]·DMA·0.28DMF·$2.9H_2O$ (BMM-11)/GCE	3D/565.33 (Langmuir)	η_{10} = 362	105.23	1.0 M KOH	OER	[39]
[$Co(II)_2(BPTC)(H_2O)(NMF)_2$]·1.29NMF·0.57MeCN/GCE	3D	η_{10} = 393	178.07	1.0 M KOH	OER	[39]
Co_2-tzpa/GCE	3D/228.7 (BET)	η_{10} = 336	58	1.0 M KOH	OER	[40]
Co_2-tzpa/GCE	3D/228.7 (BET)	η_{10} = 396	88	0.1M KOH	OER	[40]
TA-MOF/GCE	2D/670	η_1 = 382	94	13/0.1 M KOH	OER	[41]
NH_2TA-MOF/GCE	2D/720	η_1 = 356	105	13/0.1 M KOH	OER	[41]
Co-BPDC/Co-BDC-3 MOF-on-MOF heterojunction/GCE	2D/58.2 (BET)	η_{10} = 335	72.1	1.0 M KOH	OER	[42]
$Co(L)_{0.5}$(adip)/GCE	2D	η = 460	–	6.8/H_3PO_4-KOH, 0.2 M	OER	[43]
$Co_2(L)_2(5\text{-bdc})_2(H_2O)_2$·$H_2O$/GCE	2D	η = 570	–	6.8/H_3PO_4-KOH, 0.2 M	OER	[43]
{[$Co_2(L_1)_2(L_2)_2$·$(H_2O)_2]_n$·$3H_2O$}/GCE	2D/13.694 (BET)	η_{10} = 411	58	1.0 M KOH	OER	[44]
{[$Co_2(L_1)_2(L_3)_2(H_2O)_2]_n$·$4H_2O$}/GCE	2D/10.485 (BET)	η_{10} = 406	62	1.0 M KOH	OER	[44]
{[$Co(L_1)_2(HL_3)_2$]n·$2CH_3CN$}/GCE	2D/4.194 (BET)	η_{10} = 438	60	1.0 M KOH	OER	[44]
{[$Co(L_1)(HL_3)_2$·$(H_2O)_2]_n$}/GCE	1D	η_{10} = 398	59	1.0 M KOH	OER	[44]
[$Co_5(^i\text{BuOip})_4(\mu_3$-O)$(bpp)_2(DMF)(H_2O)_3$]·$2H_2O$/ NF	3D	η_{10} = 340	130	0.5M Na_2SO_4	OER	[45]
($Co(TCNQ)_2$/Co) ($Co(TCNQ)_2$ array on Co foil)/Co foil	–	η_{15} = 310	76	1.0 M KOH	OER	[46]
[$Co_{1.5}$(tib)(dcpna)]·$6H_2O$/GCE	3D	η_{10} = 360	89	1.0 M KOH	OER	[47]
Co-$MOF_{72\ h}$ (prepared by hydrothermal process for 72 h)/NF	3D/18.1 (BET)	η_{10} = 387	90	1.0 M KOH	OER	[48]
[$Co_4(BTC)_3(BIM)_6$] [solvent]/GCE	3D	η_{10} = 280	51	1.0 M KOH	OER	[49]
Ni-MOF (BTC)/CP substrate	8.39 (BET)	η_{10} = 346	64	1.0 M KOH	OER	[50]
[Co_4L_2(4,4′-bpy)$(H_2O)_6$]·$3.5H_2O$/GCE	2D	η = 460	–	6.8/H_3PO_4/KOH, 0.2 M	HER	[51]
[Co_4L_2(4,4′-bpy)$(H_2O)_6$]·$3.5H_2O$/GCE	2D	η = 430	–	6.8/H_3PO_4/KOH, 0.2 M	OER	[51]
[Co_2L(azene)$(H_2O)_3$]·DMF/GCE	3D	η = 140	–	6.8/H_3PO_4/KOH, 0.2 M	HER	[51]
[Co_2L(azene)$(H_2O)_3$]·DMF/GCE	3D	η = 230	–	6.8/H_3PO_4/KOH, 0.2 M	OER	[51]
Zn(fcdHp)/carbon paste electrode (CPE)	1D	η_{10} = 340	110	0.5 M H_2SO_4	HER	[52]
Co(fcdHp)/carbon paste electrode (CPE)	1D	η_{10} = 450	120	0.5 M H_2SO_4	HER	[52]
[$(Cu_2(HBA)_2(OH_2)$]/GCE	1D	η_{10}= 417	98	1.0 M KOH	HER	[53]
[$(Cu_2(HBA)_2$]/GCE	1D	η_{10} = 535	145	1.0 M KOH	HER	[53]
[$Cu_3(pdc)_2(phen)_2(H_2O)_2$]/carbon paste electrode (CPE)	2D/18.7	η_{10} = 440	60	1.0 M H_2SO_4	HER	[54]
[$Cu_2(NL)_2$·$4H_2O$](NTU-33 nanosheet)/GCE	2D	η_{10} = 560	158	0.5 M H_2SO_4	HER	[55]
$Co(OH)_2(C_8H_4O_4)$ (named with CoBDC)/GCE	17.12	η_{10}=378	–	1.0 M KOH	OER	[56]
CoBDC–$Fc_{0.17}$/GCE	16.03	η_{10}=291	61	1.0 M KOH	OER	[56]
CoBDC–NF/NF	–	η_{10} = 252	63	1.0 M KOH	OER	[56]
CoBDC–Fc–NF/NF	–	η_{10} = 178	51	1.0 M KOH	OER	[56]
{[Co(**L_1**)(TA)$(H_2O)_2$]·$2H_2O$}n/GCE	2D	η_1= 420	126.13	13/0.1 M KOH	OER	[57]
{[Ni(**L_1**)(TA)$(H_2O)_2$]·$2H_2O$}n/GCE	2D/80.534	η_1= 370	101.9	13/0.1 M KOH	OER	[57]
{[Co(**L_2**)$_2$(TA)]·$4H_2O$}n/GCE	2D	η_1= 430	131.66	13/0.1 M KOH	OER	[57]
{[Ni(**L_2**)$_2$(TA)]·$4H_2O$}n/GCE	2D/116.561	η_1= 400	120.53	13/0.1 M KOH	OER	[57]
Cu@{[Co(**L_1**)(TA)$(H_2O)_2$]·$2H_2O$}n/GCE	–	η_1= 410	122.19	13/0.1 M KOH	OER	[57]
Cu@{[Co(**L_2**)$_2$(TA)]·$4H_2O$}n/GCE	–	η_1= 420	123.00	13/0.1 M KOH	OER	[57]
[$Co_2(\mu\text{-OH})_2$(bbta)] (MAF-X27-OH)/GCE	3D/1514 (Langmuir)	η_{10}= 387	–	pH = 14	OER	[23]
[$Ni_4(OH)_2(NDC)_3(H_2O)_2$]/GCE	3D/4.2	η_{10}= 456	95	1.0 M KOH	OER	[58]
AB&[$Ni_4(OH)_2(NDC)_3(H_2O)_2$](1:1)/GCE	3D/38.5	η_{10}= 379	77	1.0 M KOH	OER	[58]
AB&[$Ni_4(OH)_2(NDC)_3(H_2O)_2$](1:1)/FTO (fluorine-doped tin oxide)	3D	η_{10}= 282	66	1.0 M KOH	OER	[58]
AB&[$Ni_4(OH)_2(NDC)_3(H_2O)_2$](1:1)/NF	3D	η_{10}= 263	65	1.0 M KOH	OER	[58]

GCE = glassy carbon electrode, NF = nickel foam, CP = carbon paper, CPE = carbon paste electrode, FTO = fluorine-doped tin oxide, BET = Brunauer-Emmett-Teller, AB = Acetylene black.

amperometry with 300 mV overpotential. During 12 h of electrolysis, the current density exhibits barely any degradation, proving the excellent durability of MOF against the OER. The ionization energies for the MOFs were evaluated to be 9.63 eV for Co-MOF-74, 8.27 eV for Fe-MOF-74 and 7.79 eV for $Co_{0.6}Fe_{0.4}$-MOF-74. The lowest ionization energy suggests higher electron dense surroundings given through $Co_{0.6}Fe_{0.4}$-MOF-74, which is beneficial of OER. The aforesaid observation demonstrated that iron dopants enhance the electron cloud at the cobalt atom. The production of hydroperoxy compounds may be enhanced by the higher electron cloud at the Co atom (important intermediaries for the OER). Thus, it is thought that the electron cloud transfer from iron atom to cobalt atom helps the improved OER efficiency of the heterometallic MOF. The X-ray diffraction studies suggest cobalt oxide and iron oxide were formed throughout the OER. Xia *et al.* [60] used a straightforward solvothermal approach to prepare NiFe-BDC having various dimensional structures by altering the kind and proportion of the solvent. The BET area for 2D MOF was 52.16 $m^2 g^{-1}$, which is greater in comparison to 1D MOF (37.27 $m^2 g^{-1}$) and 3D MOF (22.85 $m^2 g^{-1}$). At 10 mA cm^{-2}, 2D MOF requires 223 mV overpotential, which is less in comparison to 1D MOF (266 mV) and 3D MOF (245 mV). Compared to the values of 1D MOF (82.1 mV $decade^{-1}$) and 3D MOF (54.9 mV $decade^{-1}$), 2D MOF produces the smallest 37.3 mV $decade^{-1}$ of Tafel value. Durability for the 2D MOF is investigated through chronoamperometry. No substantial reduction of the current density was observed following 70 h of controlled potential electrolysis, indicating the exceptional OER stability for the 2D MOF. The nanosheets of the 2D MOF remain mostly undamaged, with just a little volume contraction and bending.

Cheng *et al.* [61] designed NiFe-MOF-5, by taking the reagents *viz*. $Fe(NO_3)_3{\cdot}9H_2O$, $Ni(NO_3)_2{\cdot}6H_2O$ and HCOOH in DMF medium. The MOF displays 168 mV overpotential for OER into 1 M KOH solution at 10 mA cm^{-2}. Its Tafel value is the smallest (42 mV $decade^{-1}$) and its reaction kinetics is the quickest. The current decreases only 7.7% from its initial value following 24 h of chronoamperometry experiment using a constant potential, demonstrating that MOF is a strong contender for use in real world uses. The MOF further showed quite strong HER efficiency for 163 mV overpotential into 1 M KOH solution at 10 mA cm^{-2}. Han *et al.* [62] synthesized a crystalline/amorphous-NiFe-MOF consisting of FeNi-MIL-88B crystal and NiFe-BDC powder through a carbon dioxide facilitated process. The c/a-NiFe-MOF exhibits 236 mV overpotential into 1 M KOH solution for 10 mA cm^{-2} conventional current. In comparison to c/a-NiFe-MOF, the overpotentials for NiFe-BDC, FeNi-MIL-88B and the combination of both are greater. The Ni-MOF, NiFe-BDC and FeNi-MIL-88B exhibited the highest Tafel values. The Tafel value for *c/a*-NiFe-MOF was calculated to be 30 mV $decade^{-1}$, which is the smallest between the MOFs demonstrated the efficient OER kinetics. The catalytic oxygen evolving reaction performance of c/a-NiFe-MOF may be sustained at 23 mA cm^{-2} for a minimum of 12 h and shows very slight reductions. The OER experiment resulted in the formation of catalytic nickel hydroperoxy compounds.

Zhu *et al.* [63] constructed the 2D NiFe-MOF from 2D NiFe-LDH (LDH = layered double hydroxide) through a simple solvothermal transformation. The MOF needs 260 mV overpotential at 10 mA cm^{-2}, whereas the LDH requires 338 mV into 1 M KOH. While the MOF is transformed from the LDH and deposited over nickel foam, the overpotential for OER is also decreased to 221 mV. The Tafel value for the MOF (loaded over nickel foam, 40 mV $decade^{-1}$) was substantially less compared to the LDH (loaded upon nickel foam, 48 mV $decade^{-1}$). During 20 h, no change occurred in the overpotential required to sustain a current of 10 mA cm^{-2}. Throughout the OER, the MOF progressively becomes powder. Furthermore, following OER, catalytic performance for the MOF minimally deactivates, showing that there is still significant catalytic performance in the powder compound. Lan's group [64] synthesized three heterometallic metal organic frameworks which are same and related by utilizing facile solvothermal reaction. These are formulated as $[Fe_3(\mu_3\text{-}O)(bdc)_3][Co_{2.34}(trz)_3F_2(H_2O)_{3.32}(OH^-)_{0.68}]$ (defined with Fe_3-Co_3-F_2) and $[Fe_3(\mu_3\text{-}O)(bdc)_3][Co_2(trz)_3X_2(H_2O)_4]$ (defined by Fe_3-Co_2-X_2, X = Cl, Br). The BET areas were estimated to be 477 $m^2 g^{-1}$ for F-MOF, 474 $m^2 g^{-1}$ for Cl-MOF and 329 $m^2 g^{-1}$ for Br-MOF. The F-MOF exhibits 439 mV overpotential at 10 mA cm^{-2}. The Cl-MOF has 504 mV while the Br-MOF needs 568 mV overpotential. The F-MOF has the most impressive OER efficiency and the lowest overpotential when compared to Cl-MOF and Br-MOF. In comparison to Cl-MOF (80.42 mV $decade^{-1}$) and Br-MOF (95.07 mV $decade^{-1}$), the F-MOF (76.44 mV $decade^{-1}$) exhibits a lower Tafel value demonstrated the further advantageous kinetics for OER. The plots (current *versus* time) for the three MOFs exhibit a small decrease in current during the 18 h of experiment demonstrated the better durability of three MOFs for OERs. The pre and post PXRD of the MOF loaded electrode demostrated that the simulated and experimentally obtained peaks were matched well. The aforesaid observations indicate that all the metal organic frameworks maintain their morphology and crystalline nature even following an OER. Furthermore, it is observed that roughly 98% of MOF remains attached to the electrode and the rest degrades to electrolyte, indicating the durability of MOF.

Su *et al.* [65] fabricated $A_{2.7}B$-MOF-$FeCo_{1.6}$ *via* putting together a combination of metals, terephthalic (A) and 2-aminoterephthalic ligands (B) through a solvothermal process. The BET area of the MOF was estimated to be 197.29 $m^2 g^{-1}$. It has a very good OER efficiency for 288 mV overpotential at 10 mA cm^{-2} while 301 mV overpotential is required at 20 mA cm^{-2}. The Tafel value of the MOF is 39 mV $decade^{-1}$, which shows that the process of generating hydroperoxy compounds is the rate-determination phase. Following 10 h and 33 min, the MOF showed improved durability at 10 mA cm^{-2}, despite a small overpotential rise, because of the MOF's removal from the electrode throughout the OER. Following 10 h of catalytic experiment, the crystallinity of the MOF exhibits relatively few modifications.

Chen *et al.* [21] synthesized $[\{Fe_3(\mu_3\text{-}O)(bdc)_3\}_4\{Fe(na)_4(L^T)\}_3]$ (termed Fe_3-Fe, L^T = terminal ligand) through solvothermal process of iron(II) chloride, 1,4-benzenedicaboxylic acid and nicotinic acid in DMA medium. Using dil. HCl, the

$Fe(na)_4(L^T)$ unit in Fe_3-Fe MOF was removed and $[Fe_3(\mu_3\text{-}O)(bdc)_3(L^T)_3]$ (termed Fe_3) was generated. The $[\{Fe_3(\mu_3\text{-}O)(bdc)_3\}_4\{Co_2(na)_4(L^T)_2\}_3]$ (named Fe_3-Co_2) was prepared through the reaction between the Fe_3 MOF, cobalt(II) chloride and nicotinic acid. In H_2O at pH 13 and with a conventional current of 10 mA cm^{-2}, the Fe_3-Co_2 MOF exhibits 283 mV overpotential. In H_2O of pH 13, the Tafel value of the Fe_3-Co_2 MOF is calculated to be 43 mV $decade^{-1}$. In H_2O of pH 7, catalytic efficiency for the Fe_3-Co_2 MOF was investigated and exhibited the overpotential of 431 mV at 2 mA cm^{-2} and the Tafel value obtained is 134 mV $decade^{-1}$. The Fe_3-Co_2 MOF further demonstrated excellent durability in the OER in H_2O for both pH values. The minimal alterations for linear sweep voltammetry, PXRD and XPS were found to follow the catalytic performance of 24 h.

Zhu *et al.* [66] prepared a 2D heterometallic metal organic framework MOF-Fe/Co by only stirring the combination of $FeCl_3{\cdot}6H_2O$, $Co(NO_3)_2{\cdot}6H_2O$, 1,4-benzene dicarboxylic acid and triethylamine in DMF, ethanol and water. The 2D MOF has a BET area of around 31.5 $m^2\ g^{-1}$. When OER was catalyzed by 2D MOF, 238 mV overpotential is required at 10 mA cm^{-2}. Comparing 2D MOF with bulk MOF and 3D MOF, 2D MOF has the smallest 52 mV $decade^{-1}$ of Tafel value. Thus, 2D MOF has the best catalytic performance for OER into 1 M KOH as well as the most effective reaction kinetics. The proportion of signals attributed to iron(III) enhanced following OER cycle, it is connected to the oxidation of iron(II) to iron(III) in iron hydroperoxyl throughout the oxygen formation reaction. The overpotential for 50 mA cm^{-2} rose between 285 and 298 mV when the 2D MOF was kept in the atmosphere for 30 days demonstrated the strong environmental durability of the 2D MOF. During the catalytic reaction, the 2D MOF instantly changed into cobalt oxide and iron oxide and the cobalt oxide and iron oxide exhibited excellent durability for quite some time into KOH solution. Wang *et al.* [67] generated MOFs such as a Ni-BTC (BTC = 1,3,5-trimesic acid), a Fe-BTC and a heterometallic Fe/Ni-BTC by solvothermal process. The OER electrocatalytic performance is greater in the heterometallic MOF, yet the current remains significantly less in comparison to 10 mA cm^{-2}. The heterometallic MOF is electrochemically deposited over nickel foam. The heterometallic MOF (deposited upon nickel foam) exhibits the smallest 270 mV of overpotential. The Tafel value for the heterometallic MOF (deposited over nickel foam) attains 47 mV $decade^{-1}$. Following 15 h of electrocatalytic activity, heterometallic MOF (deposited upon nickel foam) was characterized through PXRD, XPS and SEM. The crystallinity and pattern of MOF are also essentially preserved. The oxidation numbers for nickel and iron were unaltered as well. The cyclic voltammogram plots for the MOF pre and post OER were nearly similar.

Yi *et al.* [68] prepared a MOF termed with Fe_3-MOF from Fe_3 cluster $(Fe_3(\mu_3\text{-}O)(CH_3COO)_6)$ and 3,3,5,5′-azoxybenzenetetracarboxylic acid. They have also synthesized four MOFs named with Fe_2M-MOF on the basis of Fe_2M cluster (M = Ni, Co, Mn, Zn) $(Fe_2M(\mu_3\text{-}O)(CH_3COO)_6)$ and 3,3,5,5′-azoxybenzenetetracarboxylic acid. The catalytic efficiency of oxygen evolving reactions for all five MOFs was evaluated in 0.1 M KOH solution. At 10 mA cm^{-2}, the iron-cobalt MOF needs 339 mV overpotential and the iron-nickel MOF needs 333 mV overpotential. The OER efficiency of iron-cobalt MOF and iron-nickel MOF is the highest between the five MOFs. The iron-cobalt MOF has a Tafel value of 36.2 mV $decade^{-1}$ while for iron-nickel MOF, the value is 47.8 mV $decade^{-1}$. Following 24 h into 0.1 M KOH solution, the plots obtained from the chronopotentiometry experiments for iron-cobalt MOF and iron-nickel MOF show excellent durability. In 0.1 M KOH solution, the HER electrocatalytic performances for five MOFs were also examined. At 10 mA cm^{-2}, five MOFs exhibited overpotentials of 229 mV for iron-cobalt MOF, 262 mV for iron-nickel MOF, 221 mV for iron-zinc MOF, 214 mV for iron-manganese and 218 mV for iron MOF to perform HERs.

Lan *et al.* [22] synthesized four MOFs named Fe_2M-BPTC (M = Fe, Co, Ni, Zn) through reacting $Fe_2M(\mu_3\text{-}O)(CH_3COO)_6(H_2O)$ assembles and biphenyl-3,4′,5-tricarboxylic acid *via* solvothermal method, where CH_3COOH works as the opposing chemical. By measuring the overpotential of four MOFs at 10 mA cm^{-2} into 0.1 M KOH solution, the catalytic capability of four MOFs was studied. In comparison to iron MOF (555 mV), iron-cobalt MOF (376 mV) and iron-zinc MOF (522 mV), iron-nickel MOF has a smaller overpotential of 365 mV. Four MOFs exhibited Tafel values of 122.7 mV $decade^{-1}$ for iron MOF, 77.2 mV $decade^{-1}$ for iron-cobalt MOF, 81.8 mV $decade^{-1}$ for iron-nickel MOF and 121.8 mV $decade^{-1}$ for iron-zinc MOF proved that heterometallic catalysts have better kinetics for OERs. There was essentially no change between the preliminary linear sweep voltammetry plots and the following two thousand cycle linear sweep voltammetry plots for four MOFs. The plots obtained from the chronopotentiometry maintain their integrity without deterioration for at least 15 h. These observations indicated that four MOFs were extremely stable over the lengthy OER method. A method of deposition of 2D MOF from the reaction medium on diverse substrates was reported by Zhao *et al.* [69]. They have prepared iron-nickel MOF substrate using an easy chemical solution deposition process through the addition of potassium salt of 2,6-naphthalenedicarboxylic acid in water containing $Ni(CH_3COO)_2{\cdot}4H_2O$ and $Fe(NO_3)_3{\cdot}9H_2O$. The iron-nickel MOF (deposited over nickel foam) electrode has a BET area of 173 $m^2\ g^{-1}$. At 10 mA cm^{-2}, the MOF displays 240 mV overpotential into 0.1 M KOH solution to perform an OER. The iron-nickel MOF electrode's better OER efficiency is further supported through the Tafel value, which shows a lower value of 34 mV $decade^{-1}$. An extended chronoamperometry investigation lasting 5 h and 30 min validated the iron-nickel MOF electrode's exceptional durability. Against HERs, the MOF is likewise quite effective and at 10 mA cm^{-2}, it shows 134 mV overpotential in 0.1 M KOH solution.

Mai *et al.* [70] synthesized heterometallic MOFs (termed as Fe_xNi_y-BDC) through regulating the interaction and cooperation among $FeCl_3{\cdot}6H_2O$, $Ni(NO_3)_2{\cdot}6H_2O$ and 1,4-benzenedicarboxylic acid heating at 140 ºC around 4 h. The Fe:Ni has been fed in proportions of 1:0, 2:1, 1:1, 1:2, 1:4 and 0:1. While the proportion of Fe:Ni is 0:1, following the solvothermal method, nothing is produced, implying that straight

coordination of nickel with 1,4-benzenedicarboxylic acid is not possible. The catalytic efficiency of all the five MOFs against OERs was investigated into 1 M KOH solution. The smallest overpotential required by Fe_1Ni_2-BDC is 260 mV, which is considerably lower in comparison to the requirements of Fe-BDC (419 mV), Fe_2Ni_1-BDC (280 mV), Fe_1Ni_1-BDC (281 mV) and Fe_1Ni_4-BDC (280 mV). The Tafel values were found to be 76 mV decade^{-1} for Fe-BDC, 41 mV decade^{-1} for Fe_2Ni_1-BDC, 36 mV decade^{-1} for Fe_1Ni_1-BDC, 35 mV decade^{-1} for Fe_1Ni_2-BDC and 42 mV decade^{-1} for Fe_1Ni_4-BDC. It demonstrated that between the five MOFs, Fe_2Ni_1-BDC has the smallest Tafel value and thus the quickest kinetics. The TEM images for Fe_1Ni_2-BDC following 2 h of OER experiment doesn't revealed any significant changes in comparison to pure MOF. Lang *et al.* [71] generated three heterometallic metal organic frameworks Fe/Ni*x*-MIL-53 (*x* = 1.6, 2.0, 2.4) by the solvothermal methods utilizing $Ni(NO_3)_2{\cdot}6H_2O$, $FeCl_3{\cdot}6H_2O$ and 1,4-benzenedicarboxylate. The catalytic OER efficiency of three MOFs were estimated into 1 M KOH solution. At 10 mA cm^{-2}, the overpotentials for the heterometallic MOFs were 258 mV for the MOF with Fe:Ni = 1:1.6, 258 mV for the MOF with Fe:Ni = 1:2 and 244 mV for MOF with Fe:Ni = 1:2.4. These materials performed exceptionally well in OER capabilities. The Tafel values of the iron-nickel MOFs were around 40 mV decade^{-1}. They also prepared four MOFs having three metal ions (Fe/$Ni_{2.4}$/M*x*-MIL-53 (M = Co, Mn; *x* = 0.2, 0.4)) *via* the addition of a small quantity of $Co(NO_3)_2{\cdot}6H_2O$ or $Mn(NO_3)_2{\cdot}4H_2O$. Between the MOFs containing three metal ions, the MOF with Fe:Ni:Co = 1:2.4:0.4 shows the best oxygen evolving reaction capability, having 219 mV overpotential for 10 mA cm^{-2} and 236 mV overpotential for 20 mA cm^{-2}. Additional evidence of the excellent kinetics for the MOFs having three metal ions comes from the Tafel value, which shows a smallest value of 53.5 mV decade^{-1}. Following 1000 cycles, the OER plot and structure of the MOF with Fe:Ni:Co = 1:2.4:0.4 exhibited few modifications demonstrated the MOF's excellent stability. A very impressive OER capability is displayed by MOF having Fe:Ni:Mn = 1:1:0.4 developed over nickel foam, which needs 238 mV overpotential for 100 mA cm^{-2} and 290 mV over-potential for 500 mA cm^{-2}. During 60 h of electrolysis, the MOF having Fe:Ni:Mn = 1:1:0.4 maintains 93.3% of its initial current and slight variations to the structure. The characteristic parameters based on OER and HER reactions in heterometallic MOFs are summarized in Table-2.

TABLE-2
HETEROMETALLIC MOFs BASED ELECTROCATALYSTS

Electrocatalyst/Electrode	Dimension/surface area ($m^2\ g^{-1}$)	Overpotential η_x (mV), *x* = current density (mA cm^{-2})	Tafel slope (mV decade^{-1})	pH/ Electrolyte	Catalyzes	Ref.
$Co_{0.6}Fe_{0.4}$-MOF-74/GCE	3D	η_{10} = 280	56	1.0 M KOH	OER	[59]
2D-NiFe-BDC/NF	2D/52.16 (BET)	η_{10} = 223	37.3	1.0 M KOH	OER	[60]
NiFe-MOF-5	3D	η_{10} = 168	42	1.0 M KOH	OER	[61]
NiFe-MOF-5	3D	η_{10} = 163	–	1.0 M KOH	HER	[61]
c/a-NiFe-MOF/GCE	–	η_{10} = 236	30	1.0 M KOH	OER	[62]
2D NiFe MOF/GCE	2D	η_{10} = 260	40	1.0 M KOH	OER	[63]
Fe_3-Co_3-F_2/CC	3D/477(BET)	η_{10} = 439	76.44	0.1 M KOH	OER	[64]
Fe_3-Co_3-Cl_2/CC	3D/474(BET)	η_{10} = 504	80.42	0.1 M KOH	OER	[64]
Fe_3-Co_3-Br_2/CC	3D/329(BET)	η_{10} = 568	95.07	0.1 M KOH	OER	[64]
$A_{2.7}$B-MOF-$FeCo_{1.6}$/GCE	3D/197.29(BET)	η_{10} = 288	39	1.0 M KOH	OER	[65]
$[\{Fe_3(\mu_3\text{-}O)(bdc)_3\}_4\{Co_2(na)_4(L^T)_2\}_3]$/GCE	90 (BET), 215 (Langmuir)	η_{10} = 283	43	pH = 13, in Water	OER	[21]
$[\{Fe_3(\mu_3\text{-}O)(bdc)_3\}_4\{Co_2(na)_4(L^T)_2\}_3]$/GCE	90 (BET), 215 (Langmuir)	η_2 = 431	134	pH = 7, in Water	OER	[21]
MOF-Fe/Co(1:2)/GCE	2D/31.5	η_{10} = 238	52	1.0 M KOH	OER	[66]
MOF-Fe/Co(1:2)/GCE	3D	η_{10} = 311	77	1.0 M KOH	OER	[66]
Fe/Ni-BTC@NF (Fe:Ni = 1:12)/NF	–	η_{10} = 270	47	0.1 M KOH	OER	[67]
Fe_2Ni-MOF/GCE	–	η_{10} =333	47.8	1.0 M KOH	OER	[68]
Fe_2Co-MOF/GCE	–	η_{10} =339	36.2	1.0 M KOH	OER	[68]
Fe_2Zn-MOF/NF	–	η_{10} =221	174	0.1 M KOH	HER	[68]
Fe_2Ni-BPTC (NNU-23)/CC	3D	η_{10} =365	81.8	0.1 M KOH	OER	[22]
Fe_2Co-BPTC (NNU-22)/CC	3D	η_{10} =376	77.2	0.1 M KOH	OER	[22]
NiFe-MOF/NF	2D/173 (BET)	η_{10} = 240	34	0.1 M KOH	OER	[69]
NiFe-MOF/NF	2D/173 (BET)	η_{10} = 134	–	0.1 M KOH	HER	[69]
Fe_2Ni_1-BDC/GCE	–	η_{10} = 280	41	1.0 M KOH	OER	[70]
Fe_1Ni_1-BDC/GCE	–	η_{10} = 281	36	1.0 M KOH	OER	[70]
Fe_1Ni_2-BDC/GCE	–	η_{10} = 260	35	1.0 M KOH	OER	[70]
Fe_1Ni_4-BDC/GCE	–	η_{10} = 280	42	1.0 M KOH	OER	[70]
Fe/$Ni_{2.4}$/$Co_{0.4}$-MIL-53/GC	–	η_{10} = 219	53.5	1.0 M KOH	OER	[71]
Fe/$Ni_{2.4}$/$Co_{0.4}$-MIL-53/NF	–	η_{100} =238	71.3	1.0 M KOH	OER	[71]

CC = Carbon cloth.

Conclusion

Metal organic frameworks (MOFs) have hierarchical surface morphology, tuneable chemical structure, vast surface area and the existence of a large number of active sites. Furthermore, in MOFs, the catalytically active sites are uniformly dispersed metal cations. Because of their accessible pores and open channels, MOFs hold considerable promise as oxygen evolving reaction (OER) and hydrogen evolving reaction (HER) electrocatalysts, since they can accommodate electrolytes, promote reactant diffusion and help the transport/evolution of produced oxygen gas. The hostile HER and OER conditions for the 3*d*-transition MOFs could lead to the breakdown of organic ligands and the production of compounds based on water-oxidizing oxides. Therefore, investigations are required to show whether the metal organic framework truly serves as a HER and OER catalyst or not. Consequently, it is difficult to find a real metal organic framework catalyst that will directly catalyze HER or OER.

ACKNOWLEDGEMENTS

The author thanks Arun Karmakar of CSIR-Central Electrochemical Research Institute (CECRI), Karaikudi, India for the valuable scientific discussions.

CONFLICT OF INTEREST

The authors declare that there is no conflict of interests regarding the publication of this article.

REFERENCES

1. C. Xia, Q. Jiang, C. Zhao, M.N. Hedhili and H.N. Alshareef, *Adv. Mater.*, **28**, 77 (2016); https://doi.org/10.1002/adma.201503906
2. J. Luo, J.H. Im, M.T. Mayer, M. Schreier, M.K. Nazeeruddin, N.G. Park and M. Grätzel, *Science*, **345**, 1593 (2014); https://doi.org/10.1126/science.1258307
3. L. Yan, L. Cao, P. Dai, X. Gu, D. Liu, L. Li and X. Zhao, *Adv. Funct. Mater.*, **27**, 1703455 (2017); https://doi.org/10.1002/adfm.201703455
4. R. Dong, Z. Zheng, D.C. Tranca, J. Zhang, N. Chandrasekhar, S. Liu and X. Feng, *Chem. Eur. J.*, **23,** 2255 (2017); https://doi.org/10.1002/chem.201605337
5. Y. Li, S. Niu, D. Rakov, Y. Wang, M. Cabán-Acevedo, S. Zheng and P. Xu, *Nanoscale*, **10**, 7291 (2018); https://doi.org/10.1039/C8NR01811A
6. X. Zou and Y. Zhang, *Chem. Soc. Rev.*, **44**, 5148 (2015); https://doi.org/10.1039/C4CS00448E
7. X. Wen and J. Guan, *Appl. Mater. Today*, **16**, 146 (2019); https://doi.org/10.1016/j.apmt.2019.05.013
8. Y. Jiao, Y. Zheng, M. Jaroniec and S.Z. Qiao, *Chem. Soc. Rev.*, **44**, 2060 (2015); https://doi.org/10.1039/C4CS00470A
9. Y. Yan, T. He, B. Zhao, K. Qi, H. Liu and B.Y. Xia, *J. Mater. Chem. A*, **6**, 15905 (2018); https://doi.org/10.1039/C8TA05985C
10. K. Yan, T. Lafleur, J. Chai and C. Jarvis, *Electrochem. Commun.*, **62**, 24 (2016); https://doi.org/10.1016/j.elecom.2015.11.004
11. M.F. Weber and M.J. Dignam, *J. Electrochem. Soc.*, **131**, 1258 (1984); https://iopscience.iop.org/article/10.1149/1.2115797/meta
12. C.C. McCrory, S. Jung, J.C. Peters and T.F. Jaramillo, *J. Am. Chem. Soc.*, **135**, 16977 (2013); https://doi.org/10.1021/ja407115p
13. X. Zhang, Q. Liu, X. Shi, A.M. Asiri and X. Sun, *Inorg. Chem. Front.*, **5**, 1405 (2018); https://doi.org/10.1039/C8QI00163D
14. X. Zhu, X. Shi, A.M. Asiri, Y. Luo and X. Sun, *Inorg. Chem. Front.*, **5**, 1188 (2018); https://doi.org/10.1039/C8QI00119G
15. A. Corma, H.I. Garcia and F.X. Llabrés i Xamena, *Chem. Rev.*, **110**, 4606 (2010); https://doi.org/10.1021/cr9003924
16. J. Gascon, A. Corma, F. Kapteijn and F. X. Llabres i Xamena, *ACS Catal.*, **4**, 361 (2014); https://doi.org/10.1021/cs400959k
17. S. Wang and X. Wang, *Small*, **11**, 3097 (2015); https://doi.org/10.1002/smll.201500084
18. S. Wang and X. Wang, *Angew. Chem. Int. Ed.*, **55**, 2308 (2016); https://doi.org/10.1002/anie.201507145
19. J. Ryu, N. Jung, J.H. Jang, H.J. Kim and S.J. Yoo, *ACS Catal.*, **5**, 4066 (2015); https://doi.org/10.1021/acscatal.5b00349
20. J. Song, C. Wei, Z.F. Huang, C. Liu, L. Zeng, X. Wang and Z.J. Xu, *Chem. Soc. Rev.*, **49**, 2196 (2020); https://doi.org/10.1039/C9CS00607A
21. J.Q. Shen, P.Q. Liao, D.D. Zhou, C.T. He, J.X. Wu, W.X. Zhang and X.M. Chen, *J. Am. Chem. Soc.*, **139**, 1778 (2017); https://doi.org/10.1021/jacs.6b12353
22. X.L. Wang, L.Z. Dong, M. Qiao, Y.J. Tang, J. Liu, Y. Li and Y.Q. Lan, *Angew. Chem. Int. Ed.*, **57**, 9660 (2018); https://doi.org/10.1002/anie.201803587
23. X.F. Lu, P.Q. Liao, J.W. Wang, J.X. Wu, X.W. Chen, C.T. He and X.M. Chen, *J. Am. Chem. Soc.*, **138**, 8336 (2016); https://doi.org/10.1021/jacs.6b03125
24. Z. Xue, K. Liu, Q. Liu, Y. Li, M. Li, C.Y. Su, N. Ogiwara, H. Kobayashi, H. Kitagawa, M. Liu and G. Li, *Nat Commun*, **10**, 5048 (2019); https://doi.org/10.1038/s41467-019-13051-2
25. W. Cheng, X. Zhao, H. Su, F. Tang, W. Che, H. Zhang and Q. Liu, *Nat Energy*, **4**, 115 (2019); https://doi.org/10.1038/s41560-018-0308-8
26. S. Mukhopadhyay, O. Basu, R. Nasani and S.K. Das, *Chem. Commun.*, **56**, 11735 (2020); https://doi.org/10.1039/D0CC03659E
27. R. Madhu, A. Karmakar, S. Kumaravel, S.S. Sankar, K. Bera, S. Nagappan, H.N. Dhandapani and S. Kundu, *ACS Appl. Mater. Interfaces*, **14**, 1077 (2022); https://doi.org/10.1021/acsami.1c20752
28. S. Anantharaj and V. Aravindan, *Adv. Energy Mater.*, **10**, 1902666 (2019); https://doi.org/10.1002/aenm.201902666
29. K. Fan, H. Zou, Y. Lu, H. Chen, F. Li, J. Liu, L. Sun, L. Tong, M.F. Toney, M. Sui and J. Yu, *ACS Nano*, **12**, 12369 (2018); https://doi.org/10.1021/acsnano.8b06312
30. N. Han, P. Liu, J. Jiang, L. Ai, Z. Shao and S. Liu, *J. Mater. Chem. A*, **6**, 19912 (2018); https://doi.org/10.1039/C8TA06529B
31. Y. Wang, C. Xie, D. Liu, X. Huang, J. Huo and S. Wang, *ACS Appl. Mater. Interfaces*, **8**, 18652 (2016); https://doi.org/10.1021/acsami.6b05811
32. A. Tamilselvan, S. Balakumar, M. Sakar, C. Nayek, P. Murugavel and K. Saravana Kumar, *Dalton Trans.*, **43**, 5731 (2014); https://doi.org/10.1039/C3DT52260A
33. J.Y. Zhang, Y. Yan, B. Mei, R. Qi, T. He, Z. Wang, W. Fang, S. Zaman, Y. Su, S. Ding and B.Y. Xia, *Energy Environ. Sci.*, **14**, 365 (2021); https://doi.org/10.1039/D0EE03500A
34. A.M. Harzandi, S. Shadman, A.S. Nissimagoudar, D.Y. Kim, H.D. Lim, J.H. Lee, M.G. Kim, H.Y. Jeong, Y. Kim and K.S. Kim, *Adv. Energy Mater.*, **11**, 2003448 (2021); https://doi.org/10.1002/aenm.202003448
35. J. Suntivich, K.J. May, H.A. Gasteiger, J.B. Goodenough and Y. Shao-Horn, *Science*, **334**, 1383 (2011); https://doi.org/10.1126/science.1212858
36. Y. Yan, B. Xia, Z. Xu and X. Wang, *ACS Catal.*, **4**, 1693 (2014); https://doi.org/10.1021/cs500070x

37. F. Safizadeh, E. Ghali and G. Houlachi, *Int. J. Hydr. Energy*, **40**, 256 (2015); https://doi.org/10.1016/j.ijhydene.2014.10.109
38. J. Jiang, L. Huang, X. Liu and L. Ai, *ACS Appl. Mater. Interf.*, **9**, 7193 (2017); https://doi.org/10.1021/acsami.6b16534
39. L. Zhong, J. Ding, X. Wang, L. Chai, T.T. Li, K. Su and S. Huang, *Inorg. Chem.*, **59**, 2701 (2020); https://doi.org/10.1021/acs.inorgchem.9b03009
40. N. Liu, Q. Zhang and J. Guan, *Chem. Commun.*, **57**, 5016 (2021); https://doi.org/10.1039/D1CC01492G
41. S.K. Konavarapu, D. Ghosh, A. Dey, D. Pradhan and K. Biradha, *Chem. Eur. J.*, **25**, 11141 (2019); https://doi.org/10.1002/chem.201902274
42. Q. Zha, F. Yuan, G. Qin and Y. Ni, *Inorg. Chem.*, **59**, 1295 (2020); https://doi.org/10.1021/acs.inorgchem.9b03011
43. Y. Gong, H.F. Shi, Z. Hao, J.L. Sun and J.H. Lin, *Dalton Trans.*, **42**, 12252 (2013); https://doi.org/10.1039/C3DT50697E
44. D. Han, K. Huang, X. Li, M. Peng, L. Jing, B. Yu and D. Qin, *RSC Adv.*, **9**, 33890 (2019); https://doi.org/10.1039/C9RA07031A
45. Y. Zhao, Z.M. Zhai, X.Y. Liu, X.G. Yang, L.F. Ma and L.Y. Wang, *J. Solid State Chem.*, **278**, 120913 (2019); https://doi.org/10.1016/j.jssc.2019.120913
46. Y. Wei, X. Ren, H. Ma, X. Sun, Y. Zhang, X. Kuang and Q. Wei, *Chem. Eur. J.*, **24**, 2075 (2018); https://doi.org/10.1002/chem.201705606
47. Q. Meng, J. Yang, S. Ma, M. Zhai and J. Lu, *Polymers*, **9**, 676 (2017); https://doi.org/10.3390/polym9120676
48. Z. Wang, J. Chen, R. Bi, W. Dou, K. Wang, F. Mao and S. Wang, *J. Solid State Chem.*, **283**, 121128 (2020); https://doi.org/10.1016/j.jssc.2019.121128
49. R.K. Tripathy, A.K. Samantara and J.N. Behera, *Dalton Trans.*, **48**, 10557 (2019); https://doi.org/10.1039/C9DT01730E
50. V. Maruthapandian, S. Kumaraguru, S. Mohan, V. Saraswathy and S. Muralidharan, *ChemElectroChem*, **5**, 2795 (2018); https://doi.org/10.1002/celc.201800802
51. Y. Gong, Z. Hao, J. Meng, H. Shi, P. Jiang, M. Zhang and J. Lin, *ChemPlusChem*, **79**, 266 (2014); https://doi.org/10.1002/cplu.201300334
52. R. Shekurov, V.V. Khrizanforova, L. Gilmanova, M.N. Khrizanforov, V. Miluykov, O. Kataeva, Z. Yamaleeva, T. Burganov, T. Gerasimova, A. Khamatgalimov, S. Katsyuba, V. Kovalenko, Y. Krupskaya, V. Kataev, B. Büchner, V. Bon, I. Senkovs, S. Kaskelf, A. Gubaidullina, O.G. Sinyashin, Y.H. Budnikova, *Dalton Trans.*, **48**, 3601 (2019); https://doi.org/10.1039/C8DT04618B
53. P. Muthukumar, D. Moon and S.P. Anthony, *CrystEngComm*, **21**, 6552 (2019); https://doi.org/10.1039/C9CE01178A
54. D.H. He, J.J. Liu, Y. Wang, F. Li, B. Li and J.B. He, *Electrochim. Acta*, **308**, 285 (2019); https://doi.org/10.1016/j.electacta.2019.04.038
55. B. Zhou, J.J. Zheng, J. Duan, C. Hou, Y. Wang, W. Jin and Q. Xu, *ACS Appl. Mater. Interf.*, **11**, 21086 (2019); https://doi.org/10.1021/acsami.9b04471
56. Z. Xue, K. Liu, Q. Liu, Y. Li, M. Li, C.Y. Su, N. Ogiwara, H. Kobayashi, H. Kitagawa, M. Liu and G. Li, *Nat Commun*, **10**, 5048 (2019); https://doi.org/10.1038/s41467-019-13051-2
57. A. Goswami, D. Ghosh, V.V. Chernyshev, A. Dey, D. Pradhan and K. Biradha, *ACS Appl. Mater. Interf.*, **12**, 33679 (2020); https://doi.org/10.1021/acsami.0c07268
58. X. Wang, B. Li, Y.P. Wu, A. Tsamis, H.G. Yu, S. Liu, J. Zhao, Y.S. Li and D.S. Li, *Inorg. Chem.*, **59**, 4764 (2020); https://doi.org/10.1021/acs.inorgchem.0c00024
59. X. Zhao, B. Pattengale, D. Fan, Z. Zou, Y. Zhao, J. Du and C. Xu, *ACS Energy Lett.*, **3**, 2520 (2018); https://doi.org/10.1021/acsenergylett.8b01540
60. K. Yue, J. Liu, C. Xia, K. Zhan, P. Wang, X. Wang and B.Y. Xia, *Mater. Chem. Front.*, **5**, 7191 (2021); https://doi.org/10.1039/D1QM00960E
61. Q. Mou, Z. Xu, G. Wang, E. Li, J. Liu, P. Zhao and G. Cheng, *Inorg. Chem. Front.*, **8**, 2889 (2021); https://doi.org/10.1039/D1QI00267H
62. Y. Li, W. Ma, H. Yang, Q. Tian, Q. Xu and B. Han, *Chem. Commun.*, **58**, 6833 (2022); https://doi.org/10.1039/D2CC01163H
63. Y. Liu, X. Li, Q. Sun, Z. Wang, W.H. Huang, X. Guo and Z. Zhu, *Small*, **18** 2201076 (2022); https://doi.org/10.1002/smLl.202201076
64. J.N. Lu, J. Liu, L.Z. Dong, S.L. Li, Y.H. Kan and Y.Q. Lan, *Chem. Eur. J.*, **25**, 15830 (2019); https://doi.org/10.1002/chem.201903482
65. Z. Xue, Y. Li, Y. Zhang, W. Geng, B. Jia, J. Tang, S. Bao, H.-P. Wang, Y. Fan, Z. Wei, Z. Zhang, Z. Ke, G. Li and C.Y. Su, *Adv. Energy Mater.*, **8**, 1801564 (2018); https://doi.org/10.1002/aenm.201801564
66. K. Ge, S. Sun, Y. Zhao, K. Yang, S. Wang, Z. Zhang, J. Cao, Y. Yang, Y. Zhang, M. Pan and L. Zhu, *Angew. Chem. Int. Ed.*, **60**, 12097 (2021); https://doi.org/10.1002/anie.202102632
67. L. Wang, Y. Wu, R. Cao, L. Ren, M. Chen, X. Feng and B. Wang, *ACS Appl. Mater. Interf.*, **8**, 16736 (2016); https://doi.org/10.1021/acsami.6b05375
68. M. Gu, S.C. Wang, C. Chen, D. Xiong and F.Y. Yi, *Inorg. Chem.*, **59** 6078 (2020); https://doi.org/10.1021/acs.inorgchem.0c00100
69. J. Duan, S. Chen and C. Zhao, *Nat. Commun.*, **8**, 15341 (2017); https://doi.org/10.1038/ncomms15341
70. J. Li, W. Huang, M. Wang, S. Xi, J. Meng, K. Zhao, J. Jin, W. Xu, Z. Wang, X. Liu, Q. Chen, L. Xu, X. Liao, Y. Jiang, K.A. Owusu, B. Jiang, C. Chen, D. Fan, L. Zhou and L. Mai, *ACS Energy Lett.*, **4**, 285 (2019); https://doi.org/10.1021/acsenergylett.8b02345
71. F.L. Li, Q. Shao, X. Huang and J.P. Lang, *Angew. Chem. Int. Ed.*, **130**, 1906 (2018); https://doi.org/10.1002/ange.201711376